Earth and Planetary Science Letters 430 (2015) 356–366

Contents lists available at ScienceDirect

Earth and Planetary Science Letters

www.elsevier.com/locate/epsl

Modeling the effect of subgrain rotation recrystallization on the evolution of olivine crystal preferred orientations in simple shear

Javier Signorelli [a,*], Andréa Tommasi [b]

[a] Instituto de Física Rosario, CONICET – Universidad Nacional de Rosario, Bv. 27 de Febrero 210 bis, Rosario, Argentina
[b] Géosciences Montpellier – CNRS & Université de Montpellier, Place Eugene Bataillon, Montpellier, France

ARTICLE INFO

Article history:
Received 9 December 2014
Received in revised form 5 August 2015
Accepted 15 August 2015
Available online xxxx
Editor: Y. Ricard

Keywords:
olivine
viscoplasticity
recrystallization by subgrain rotation
CPO development

ABSTRACT

Homogenization models are widely used to predict the evolution of texture (crystal preferred orientations) and resulting anisotropy of physical properties in metals, rocks, and ice. They fail, however, in predicting two main features of texture evolution in simple shear (the dominant deformation regime on Earth) for highly anisotropic crystals, like olivine: (1) the fast rotation of the CPO towards a stable position characterized by parallelism of the dominant slip system and the macroscopic shear and (2) the asymptotical evolution towards a constant intensity. To better predict CPO-induced anisotropy in the mantle, but limiting computational costs and use of poorly-constrained physical parameters, we modified a viscoplastic self-consistent code to simulate the effects of subgrain rotation recrystallization. To each crystal is associated a finite number of fragments (possible subgrains). Formation of a subgrain corresponds to introduction of a disorientation (relative to the parent) and resetting of the fragment strain and internal energy. The probability of formation of a subgrain is controlled by comparison between the local internal energy and the average value in the polycrystal. A two-level mechanical interaction scheme is applied for simulating the intracrystalline strain heterogeneity allowed by the formation of low-angle grain boundaries. Within a crystal, interactions between subgrains follow a constant stress scheme. The interactions between grains are simulated by a tangent viscoplastic self-consistent approach. This two-level approach better reproduces the evolution of olivine CPO in simple shear in experiments and nature. It also predicts a marked weakening at low shear strains, consistently with experimental data.

1. Introduction

Crystal preferred orientations (CPO) are ubiquitous in rocks deformed by ductile processes. They attest for the importance of dislocation creep in the deformation of the Earth. They also result in anisotropy of physical properties in the Earth crust and mantle. Indeed, most rock-forming minerals have strongly anisotropic physical properties. Development in response to flow of a preferred orientation of the crystals transfers this anisotropy to larger scales. The ubiquitous measurement of anisotropic propagation of seismic waves using teleseismic shear waves or surface waves is an evidence for this upscaling. It implies that the elastically anisotropic of olivine crystals that compose most of the upper mantle have consistent preferred orientations at scales of tens to hundreds of km (Mainprice, 2007).

Thermal diffusion and viscoplastic deformation of olivine are also anisotropic (Kobayashi, 1974; Chai et al., 1996; Tommasi et al., 2001; Durham and Goetze, 1977; Bai et al., 1991; Hansen et al., 2012a). Existence of preferred orientation of olivine crystals at large scale should therefore result in an anisotropic thermo-mechanical behavior of the upper mantle. Numerical models of lithospheric deformation that explicitly consider an evolving CPO-induced mechanical anisotropy display indeed strain localization depending on the orientation of the olivine CPO relatively to the applied stresses (Knoll et al., 2009; Tommasi et al., 2009). They also show a high sensitivity of the strain distribution to the evolution of the CPO (Tommasi et al., 2009). Accurate modeling of the upper mantle deformation requires therefore correct prediction of the olivine CPO evolution.

A variety of homogenization models, ranging from kinematic (Etchecopar, 1977; Etchecopar and Vasseur, 1987; Ribe, 1989; Kaminski and Ribe, 2001) to lower bound (Chastel et al., 1993),

* Corresponding author.
E-mail address: signorelli@ifir-conicet.gov.ar (J. Signorelli).
URLs: http://www.ifir-conicet.gov.ar (J. Signorelli), http://www.gm.univ-montp2.fr (A. Tommasi).

http://dx.doi.org/10.1016/j.epsl.2015.08.018
0012-821X/

tangent viscoplastic self-consistent (TGT-VPSC; Wenk et al., 1991; Tommasi et al., 1999, 2000), and second order viscoplastic self-consistent (SO) approaches (Castelnau et al., 2008; Raterron et al., 2014), have been used to calculate the evolution of olivine crystal preferred orientation and the resulting anisotropy of physical properties in the mantle. These models fail, however, in predicting the essential features of the olivine CPO evolution in simple shear: (1) the fast reorientation towards a stable position characterized by parallelism of the dominant slip system and the macroscopic shear at shear strains as low as 2 and (2) the asymptotical behavior of the CPO intensity, which remains almost constant for shear strains $\geq$5. This characteristic evolution is well documented in simple shear experiments on olivine polycrystals at high temperature and moderate pressure conditions (Zhang and Karato, 1995; Bystricky et al., 2000; Demouchy et al., 2012; Hansen et al., 2014). It also corroborated by the analysis of the olivine CPO in shear zones in peridotite massifs (e.g., Warren et al., 2008) and by the limited range of CPO intensities in naturally deformed peridotites (Ben Ismaïl and Mainprice, 1998; Tommasi et al., 2000).

This CPO evolution in simple shear is shared by other highly anisotropy crystalline materials, like ice (Bouchez and Duval, 1982) and quartzites deformed under low temperature or high strain rates conditions (Schmid and Casey, 1986; Dell'Angelo and Tullis, 1989). These three materials have few slip systems with highly contrasted critical resolved shear stresses and need therefore the assistance of diffusion-based mechanisms to accommodate a general deformation. They are also characterized by highly heterogeneous inter- and intragranular strain and stress distributions, as illustrated by digital image correlation data of deformation experiments in ice polycrystals, which show strain concentrations at both grain boundaries and low-angle tilt boundaries that crosscut the crystals (Grennerat et al., 2012).

Analysis of deformed peridotites highlights similar features in olivine. Deformed crystals are crosscut by numerous low-angle tilt boundaries parallel to the (100) plane. Analysis of the misorientation across these boundaries and TEM data shows that they are essentially composed by dislocations of the [100]{0kl} systems (e.g., Green and Radcliffe, 1972; Buiskool Toxopeus and Boland, 1976; Falus et al., 2011). Deformation bands with misorientations ranging from 8 to 32° were also observed in deformation experiments on olivine single crystals where the available slip systems could not accommodate the fixed boundary conditions at the contact with the pistons (Demouchy et al., 2013). These observations suggest that formation of low-angle grain boundaries is an essential strain accommodation feature in highly anisotropic materials.

Dynamic recrystallization by subgrain rotation (Poirier and Nicolas, 1975) or nucleation and growth (migration recrystallization, Guillope and Poirier, 1979) has been traditionally proposed to explain this discrepancy in CPO evolution between models and observations. Indeed, when the CPO of parent and recrystallized grains could be measured separately, the latter shows a higher dispersion (Nicolas et al., 1973; Tommasi et al., 2000; Zhang et al., 2000; Falus et al., 2011). This suggests that dynamic recrystallization contributes to weaken the CPO. The link between dynamic recrystallization and the parallelism between the dominant slip system and the macroscopic shear is less clear. However, kinematic models of CPO evolution that simulate the recrystallization by a fragmentation of the crystals restoring isometric shapes (Etchecopar, 1977; Etchecopar and Vasseur, 1987) do reproduce correctly the CPO evolution of ice in simple shear (Bouchez and Duval, 1982).

More recent polycrystal plasticity models incorporating dynamic recrystallization (Wenk and Tomé, 1999; Kaminski and Ribe, 2001) have focused on the nucleation and growth recrystallization. They were able to reproduce the experimental simple shear CPOs of olivine polycrystals by assuming that crystals in soft orientations will recrystallize earlier, producing undeformed nuclei with the same orientation, and that fast growth of these nuclei will lead this orientation to dominate the final CPO. However, these models are highly sensitive to ad-hoc parameters, which control the effectiveness of nucleation and grain growth. Experimental data constraining these parameters, which should be both stress and temperature dependent, are lacking. The parameters were therefore fitted to reproduce the experimental data in simple shear. However, this results in different CPO evolutions for geodynamic settings in which flow direction changes rapidly, as beneath an oceanic ridge (Castelnau et al., 2009). If these models are coupled to geodynamic simulations, such variations will translate in markedly different viscoplastic anisotropies and, hence, flow patterns.

The aim of the present study is to produce a simple, but robust model predicting the evolution of olivine CPO in simple shear, which will allow more precise modeling of the effect of CPO-induced viscoplastic anisotropy of olivine on geodynamic flows. We opted to investigate an alternative recrystallization process: continuous dynamic recrystallization (CDRX), focusing on the consequences of the formation of subgrains on the CPO evolution and mechanical behavior of an olivine polycrystal deformed in simple shear. This choice is justified by microstructural observations in naturally and experimentally deformed peridotites, like the high proportion of low-angle grain boundaries with misorientations accommodated by rotations around {0kl} axes and the predominance of recrystallized grains with sizes similar to the subgrains (e.g., Falus et al., 2011), which suggest that, in olivine-rich rocks, nucleation during dynamic recrystallization occurs essentially by progressive misorientation of low-angle boundaries.

2. The model

We have extended the TGT-VPSC code to simulate the effect of CDRX on the CPO evolution. The proposed CDRX scheme considers the effects of formation of subgrains (polygonalization of the crystals) on both the CPO evolution and the mechanical behavior of the crystals. It has a limited number of parameters and may be easily transferred to other linearization methods, like the second-order VPSC approach (e.g., Castelnau et al., 2008).

2.1. Modeling CDRX

In CDRX the microstructure evolves by progressive fragmentation of the grains. First, dislocations organize themselves into low-angle boundaries (LAB), leading to formation of subgrains (polygonization). Continued dislocation accumulation results in progressive increase of the misorientation at the LAB, which evolve into high-angle boundaries (HAB), completing the recrystallization process. Inspired by the early works of Etchecopar (1977) and Etchecopar and Vasseur (1987), the more recent model by Gourdet and Montheillet (2003), and by the observations described previously, we propose the following approach in order to simulate CDRX.

We assume that the grains are initially homogeneous, but that during CDRX they may fragment into, at most, n subgrains (called in the following fragments). The creation of a subgrain may only occur if: (i) the strain accumulated in the parent has reached a threshold ϵ_0 and (ii) the local (parent) stored energy $E_j^{g,(k)}$ is higher than the polycrystal average $\overline{E}^{(k)}$ (nucleation conditions). As subgrains are observed even in olivine polycrystals submitted to very low strains (e.g., Bystricky et al., 2000; Skemer et al., 2011), the strain threshold in the reference model was arbitrarily set to 0.25, but we also tested strain thresholds of 0.125 and 1 (Supplementary Material Fig. S1a–b). The local $E_i^{g,(k)}$ and polycrystal $\overline{E}^{(k)}$

stored energy are assumed to be proportional to either the crystal plastic work or the crystal plastic work rate. Both assumptions consider that the internal energy is directly linked to the dislocation population in the crystal, which depends on both the local stress and strain (or strain rate). The second option considers that effective recovery allows for fast re-equilibration of the dislocation microstructure, which records therefore solely the last strain increment. It is consistent with the steady-state behavior observed in deformation experiments in olivine crystals at high temperature (≥1200 °C, Bai et al., 1991).

The probability of nucleation follows a simplification of the criteria given in Solas et al. (2001), where the value of the constant E_2 determines the efficiency of nucleation process.

$$p_i^{g,(k)} = \begin{cases} 1 - \exp\left(-\frac{E_i^{g,(k)} - \bar{E}^{(k)}}{E_2 \bar{E}^{(k)}}\right) & \text{if } E_i^{g,(k)} > \bar{E}^{(k)};\ \Delta\varepsilon_i^{g,(k)} > \epsilon_0;\ w_i^g \neq 0, \\ 0 \quad \text{else} \end{cases} \tag{1}$$

When the nucleation probability factor, $p_i^{g,(k)}$, $i = 1, \ldots, n-1$, exceeds a randomly generated number between 0 and 1, nucleation takes place. Most simulations were run using an arbitrary value of E_2 of 2, but tests using different E_2 values show similar CPO and mechanical evolutions (Supplementary Material Fig. S1c–d). A drawback of the current implementation of CDRX is that the nucleation kinetics depends on the applied deformation step $\Delta\varepsilon$. Similar nucleation probabilities and, hence, similar CPO evolutions in models with different deformation steps may nevertheless be obtained by correcting the probability function as:

$${}_{\Delta\varepsilon} p_i^{g,(k)} = 1 - \sqrt[N]{1 - {}_{\Delta\varepsilon_{ref}} p_i^{g,(k)}}, \tag{2}$$

where $\Delta\varepsilon$ and $\Delta\varepsilon_{ref}$ are the current and the reference strain increments and $N = \Delta\varepsilon_{ref}/\Delta\varepsilon$ (Supplementary Material Fig. S1e–f).

Initially the entire volume fraction is assigned to the parent fragment (i.e., $w_0^g = w^g$, where w^g is the volume fraction of the whole grain g); the other fragments have a null volume fraction ($w_i^g = 0$ for $i = 1, \ldots, n-1$). Creation of a subgrain corresponds to the transfer of a volume fraction $w_i^g = \frac{1}{n} w^g$ from the initial parent to one of the unused fragments (i.e., those with a null volume fraction, $w_i^g = 0$):

$$w_p^{g,(k)} = w_p^{g,(k-1)} - w_i^g, \tag{3}$$

where the superindex k refers to the deformation step in which the subgrain is created. When all fragments are used, a new fragment is created by resetting the data of one of the existing fragments, chosen randomly among the n possible sites. Fig. 1a illustrates schematically how the model accounts for the evolution of the volume fractions of between parents and newly formed subgrains. Tests on the consequences of imposing a fixed number of possible fragments show that 10 fragments suffice to capture in a statistic way the steady-state crystal orientation distribution and the associated strain heterogeneity due to CDRX (Supplementary Material Fig. S1g–h).

In the first step, only the initial parent grain may give rise to a subgrain, because $w_i^g = 0$ for $i \geq 1$. However, once created, all fragments are potential parents. When more than one fragment verifies the condition (1), only the fragment displaying the maximum internal energy nucleates. The weight transfer is made from the initial parent towards the new subgrain, until the parent attains a volume fraction $w_i^g = \frac{1}{n} w^g$. Afterwards, no weight transfer is made, but the accumulated strain, the local work, and the orientation of the new subgrain are updated as follows.

The new fragment accumulated strain and plastic work are set to zero, $\Delta\varepsilon_i^{g,(k)} = 0$. Its orientation is calculated by rotating the parent orientation by an angle ϑ_j around an axis defined as:

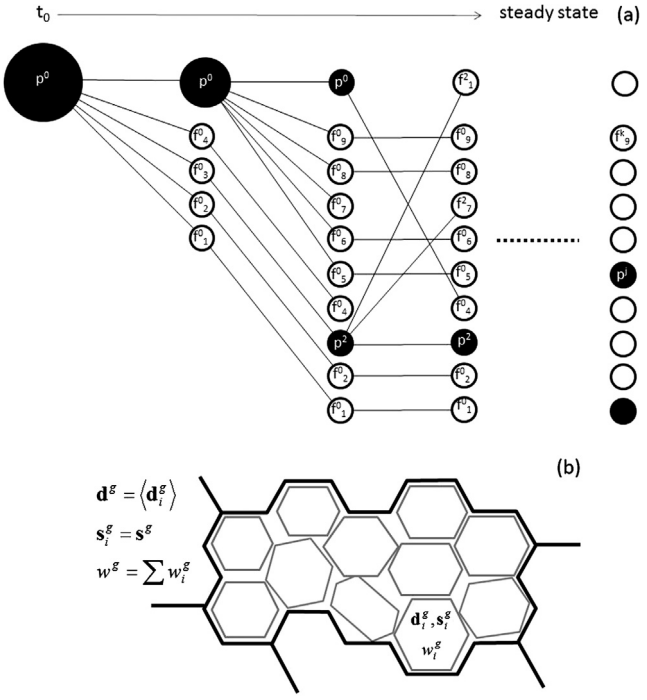

Fig. 1. Schema of the composite-grain continuous dynamic recrystallization (CDRX-CG) model. (a) Weight redistribution between parents and subgrains during CDRX. At t_0, the entire volume fraction of the grain is assigned to the parent p^0. At the end of each deformation step, if the recrystallization criteria are fulfilled, one recrystallization event occurs (the fragment with the highest internal energy recrystallizes, independently if it was a parent or a subgrain in the previous step). This results in progressive transfer of weight from the parent to the subgrains (f_n^i, where the superscript indicates the parent and the subscript, the subgrain), until all n possible fragments ($n = 10$ in the reference model) are filled. Subsequently (i.e., after the first $n-1$ nucleation events), the new subgrain is created by resetting the data of one of the existing fragments chosen randomly among the n possible sites. (b) Schema of the mechanical interactions within a grain. Each grain is composed by a finite number of subgrains, which are misoriented by an angle $-\vartheta^0 \leq \vartheta_j \leq \vartheta^0$. The interactions between the subgrains follow a lower bound model, implying that the local stresses s_i^g are constant in all subgrains, but that the local (subgrains) strain rates d_i^g may vary freely. The grain strain rate d^g is the average of the subgrain strain rates and the grain weight w^g is the sum of the subgrain weights w_i^g. Within a subgrain, stresses s_i^g and strain rates d_i^g are constant.

$$\overline{\mathbf{UVW}}_j^{g,(k)}, \vartheta_j^{g,(k)} = \frac{1}{\sum_{sys} |\gamma_{j,sys}^{g,(k)}|} \sum_{sys} \bar{\mathbf{n}}_{j,sys}^{g,(k)} \otimes \bar{\mathbf{b}}_{j,sys}^{g,(k)} |\gamma_{j,sys}^{g,(k)}|,$$
$$-\vartheta^0 \leq \vartheta_j \leq \vartheta^0 \; rnd, \tag{4}$$

where $\bar{\mathbf{b}}$ is the slip plane direction or Burgers vector, $\bar{\mathbf{n}}$ is the slip plane normal direction. This assumption considers that the subgrains are limited by tilt walls composed by edge dislocations of the active slip systems in a proportion that is equivalent to their activity. This hypothesis is justified by TEM data showing that the LAB in olivine are essentially (100) tilt boundaries, composed by edge dislocations of the [100](010) and [100](001) systems (e.g., Green and Radcliffe, 1972; Buiskool Toxopeus and Boland, 1976). It is also corroborated by the analysis of the rotation axes accommodating misorientations across LAB in olivine from naturally deformed peridotites, which are mainly of <0VW> type, consistently with the dominant activation of [100]{0kl} systems inferred from the analysis of the CPO (e.g., Tommasi et al., 2008; Soustelle et al., 2010; Zaffarana et al., 2014). However, we also tested the effect of imposing a random rotation axis (Supplementary Material Fig. S1i–j).

At each subgrain formation event, we impose a random misorientation angle $-\vartheta^0 \leq \vartheta_j \leq \vartheta^0$. This procedure results in a statistical LAB misorientation distribution similar to the one resulting from continuous creation of subgrains with low misorientations

and progressive increase of the misorientation by accumulation of dislocations within the existing subgrains. In most models, the maximum possible disorientation, ϑ^0, is $\pm 15°$, which is the usually assumed limit between a low (subgrain) and a high angle (grain) boundary in minerals, but a higher value of $\pm 30°$ was also tested (Supplementary Material Fig. S1k–l).

The actual recrystallization, that is the transformation of a LAB into a HAB, is modeled implicitly by considering that the HAB and corresponding orientations are statistically represented in the global CPO. This assumption implies that the recrystallized grains are mechanically independently of the parent crystal and, by consequence, only submitted to long-range interactions (cf. Section 2.2).

2.2. Mechanical interactions within and between grains

We use a two-level mechanical interaction scheme for simulating the mechanical consequences of the CDRX. Within a crystal, interactions between subgrains follow a constant stress scheme. A modified tangent viscoplastic self-consistent approach simulates the interactions between grains.

2.2.1. Short-range (intracrystalline) interactions: Composite Grain (CG) model

The formation of LAB allows for intracrystalline strain heterogeneity. We use a Composite Grain (CG) model to simulate this effect (Fig. 1b). The CG model considers the grain as an ensemble of subgrains with slightly different crystallographic orientations, which are related to each other by short-range interactions. It is based on the relaxed constraints theory (Honneff and Mecking, 1981) and is frequently used to simulate coupled deformation between two crystalline domains separated by a planar interface, such as twins (Lebensohn et al., 1998; Proust et al., 2007).

Assuming that the stress $\mathbf{s}_i^g$ and the strain rate $\mathbf{d}_i^g$ are homogeneous within each subgrain (fragment), the stresses and strain rates at grain level are given by the weighted average:

$$\mathbf{d}^g = \sum_i w_i^g \mathbf{d}_i^g \tag{5a}$$

$$\mathbf{s}^g = \sum_i w_i^g \mathbf{s}_i^g, \tag{5b}$$

where i runs over all fragments that form the composite grain ($i = 1, \ldots, 10$ in the reference case). Using the rate-sensitivity equation to describe the crystal plasticity, Eq. (5a) can be rewritten as:

$$\mathbf{d}^g - \dot{\gamma}_0 \sum_i w_i^g \left(\sum_{sys} \mathbf{m}_{i,sys}^g \left(\frac{\mathbf{m}_{i,sys}^g \mathbf{s}_i^g}{\tau_c^{sys}} \right)^n \right) = 0, \tag{6}$$

where $\mathbf{m}$ is the symmetric part of the Schmid orientation tensor. In the present models, we assume that the interaction between the subgrains follows an equilibrium-based model, where the stress is constant in all fragments ($\mathbf{s}_i^g = \mathbf{s}^g$). This pragmatic approach allows avoiding the definition of an explicit interface between pairs of fragments and results in major simplification in the computational treatment. In addition, this assumption allows for maximum strain heterogeneity within the grain.

2.2.2. Long-range (polycrystal-scale) interactions: modified TGT-VPSC model

By considering each CG in the polycrystal as an inclusion embedded in an equivalent medium, it is possible to extend the TGT-VPSC 1-site interaction equation (Lebensohn and Tomé, 1993). This produces, for each CG, the following system of nonlinear equations:

Table 1
Slip systems' data for olivine deformation at high-temperature, moderate pressure, dry conditions: slip plane and Burgers vector, Critical Resolved Shear Stress (CRSS), and stress exponent. Systems marked by (*) are used for numerical convenience and for the sake of having 5 independent slip systems available; they accommodate <0.1% of the total deformation at any step in all models, except in the second order VPSC where these systems accommodate >5%, reaching up to 22%, of the total strain rate at shear strains higher than 2.

Slip system	CRSS	n
(010)[100]	1	3
(001)[100]	1	3
(010)[001]	2	3
(100)[001]	4	3
{011}[100]	4	3
{111}[110]*	50	3
{111}[011]*	50	3

$$\bar{\mathbf{d}} + \tilde{\mathbf{M}}\bar{\mathbf{s}} - \dot{\gamma}_0 \sum_i w_i^g \left(\sum_{sys} \mathbf{m}_{i,sys}^g \left(\frac{\mathbf{m}_{i,sys}^g \mathbf{s}_i^g}{\tau_c^{sys}} \right)^n \right) - \tilde{\mathbf{M}}\mathbf{s}^g = 0$$

$$\mathbf{s}_i^g = \mathbf{s}^g, \tag{7}$$

where $\tilde{\mathbf{M}}$ is the interaction tensor, which is function of the viscoplastic Eshelby tensor and the macroscopic tangent compliance, and $\bar{\mathbf{d}}$, $\bar{\mathbf{s}}$ are the polycrystal (macroscopic) strain rate and stress. The tangent compliance of the CG structure, $\mathbf{M^g}$, can be calculated from the tangent compliance of the fragments that compose it, $\mathbf{M}_i^g$.

The self-consistent assumption is used to determine the strain partitioning between all CG structures in the aggregate. After numerical convergence is achieved (<0.1% deviation between local and global stresses and strain rates), the reorientation of each fragment of the CG is evaluated. The lattice rotation rate is given by:

$$\mathbf{w}_i^g = \mathbf{W} - \sum_s \mathbf{q}_{i,sys}^g \dot{\gamma}_{i,sys}^g + \tilde{\mathbf{w}}^g, \tag{8}$$

where $\mathbf{W}$ is the antisymmetric component of the imposed macroscopic velocity gradient, the second term is the plastic spin associated with each fragment, and $\tilde{\mathbf{w}}^g$ is the reorientation rate of the associated ellipsoidal inclusion.

3. Olivine CPO evolution in the CDRX-CG model

Olivine has only 3 independent systems, which critical resolved shear stresses (CRSS) depend on the deformation conditions (stress, pressure, water fugacity; e.g., Durham and Goetze, 1977; Jung and Karato, 2001; Mainprice et al., 2005; Demouchy et al., 2013). Since the present models are tested by comparison with simple shear data from high temperature, moderate pressure, dry experiments, we impose in all models [100](010) as the easiest system, followed by [100](010). [001]{hk0} systems are harder. The full slip systems' data are listed in Table 1. In all simulations, 500 grains are used and each grain may fragment into 10 subgrains. The input parameters that control the efficiency of recrystallization and the orientation of the subgrains relative to the parents in the CDRX-CG model are listed in Table 2.

Fig. 2 illustrates the predicted CPO evolution with increasing shear strain for an initially random olivine polycrystal in a CDRX-CG model where the stored energy is assumed proportional to the plastic work. Already at shear strains of 0.5, the model predicts a weak but clear CPO with a roughly orthorhombic symmetry. This CPO is characterized by alignment of the maximum concentration of [100] and [010] with the maximum and minimum finite strain ellipsoid axes, respectively. For shear strains >2, the CPO starts to rotate faster than the finite strain ellipsoid. At shear strains of 5, the maximum concentrations of [100] and [010] are subparallel (<7°) to the imposed shear direction and normal to the shear

Table 2
Input parameters in the CDRX-CG model.

Parameter	Value in reference model	Other values tested
# fragments	10	5; 20
Strain threshold E0	0.25	0.125; 1.0
Nucleation efficiency E_2	3.0	1.5; 5.0
Rotation axis [UVW]	function of slip systems activity	random
Maximum rotation angle	±15°	±30°
Incremental step	0.01	0.001; 0.005

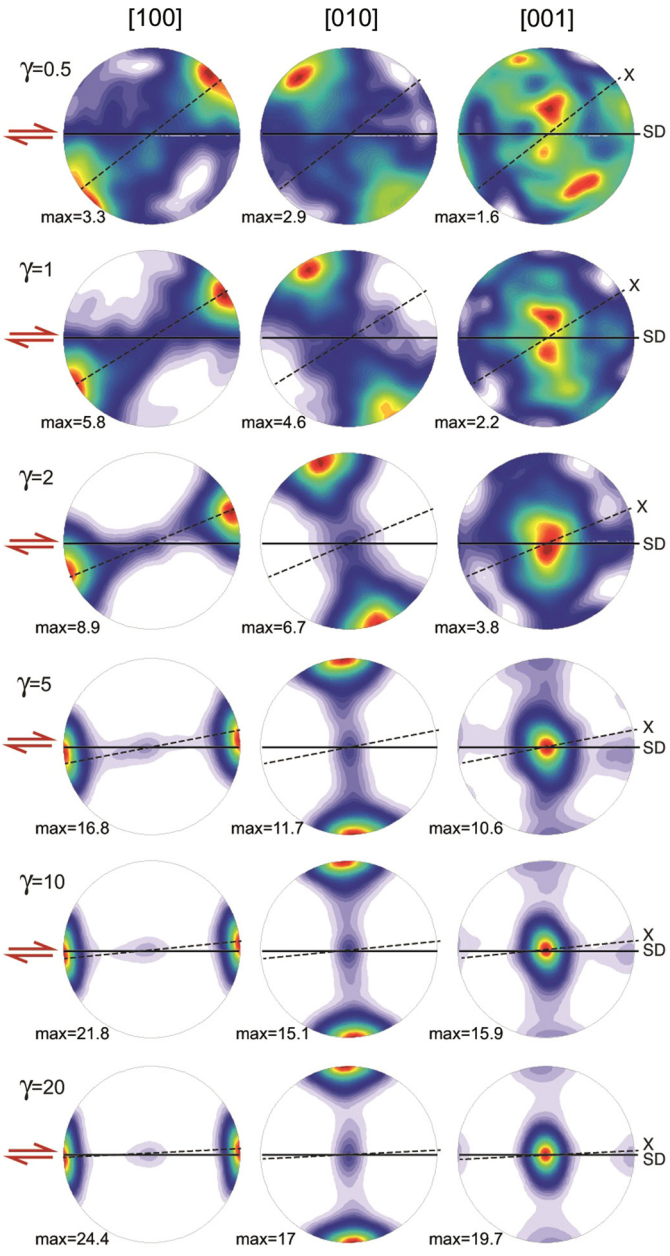

Fig. 2. CPO evolution with increasing shear strain (γ) in the CDRX-CG model. Lower hemisphere stereographic plots. SD = shear direction; X = maximum finite stretching direction (lineation); Z = maximum finite shortening direction (normal to the foliation). The continuous black line marks the shear plane, the dashed one, the foliation (plane normal to the minimum finite stretching direction).

plane, respectively. In addition, [001] becomes more concentrated, forming a well-developed single maximum in the shear plane, normal to the shear direction. For shear strains ≥10, the maximum concentration of [100] forms an angle of ~3° to the shear direction. This CPO remains stable both in orientation and intensity up to shear strains of 20 and higher.

Comparison between the CPO of the non-recrystallized grains (that never formed a subgrain) and of the recrystallized ones (in which at least one subgrain formation event occurred) highlights the effect of the CDRX-CG model on the CPO evolution (Fig. 3). The CPO of the non-recrystallized grains is characterized, at all strains, by strong maxima of [100] and [010] aligned with the maximum and minimum elongation directions of the finite strain ellipsoid, respectively. In contrast, the CPO of the recrystallized grains rotates faster than the finite strain ellipsoid. Parallelism between the [100] maximum and the shear direction is attained at shear strains <5 and this orientation remains stable thereafter. The evolution of the intensity of the CPO also differs. It is faster in the non-recrystallized population.

Simulations using a work rate-based nucleation criterion show qualitatively similar results, but a faster re-orientation of the CPO (Fig. 4a). This faster rotation of the CPO towards alignment of the [100] maximum with the shear direction is due to the more effective subgrain formation in these simulations. Indeed, at a shear strain of 2, 69% of the grains have already recrystallized in the work rate-based simulations, compared to 56% in the work-based models (Fig. 4a). For shear strains ≥7, the two models show similar behaviors. The more effective recrystallization in the work rate-based models at low strains also results in a slower evolution of the CPO intensity, resulting in slightly lower asymptotic values (Fig. 4b).

In summary, the main prediction of the CDRX-CG models, which is a fast evolution of the CPO towards a stable CPO with well-developed maxima of [100] and [010] parallel to the shear direction and normal to the shear plane, respectively, does not depend on whether the nucleation is controlled by contrasts of plastic work or work rate. More effective formation of subgrains in the work rate-based simulations results in a faster rotation of the CPO. However, the maximum difference in orientation between the two models is ca. 4° at a shear strain of 5. Model predictions also show a very weak sensitivity to the numerical parameters controlling the nucleation rate (critical strain and probability factor) and the reorientation of the fragments during nucleation (rotation angle and axis) as illustrated in Supplementary Material Fig. S1. The asymptotic value of the CPO intensity is slightly lower for more effective recrystallization; the maximum reduction (by a factor 2) is associated with the use of a larger misorientation range. The rate of rotation of the CPO is even less sensitive to the nucleation parameters, but use of random rotation axes delays the reorientation of the CPO.

4. Comparison to olivine CPO evolution in simple shear experiments and a natural shear zone

Fig. 4 compares the CPO evolution (orientation and strength) predicted by CDRX-CG models with data for olivine polycrystals deformed in simple shear at high temperature and moderate pressure conditions (Zhang and Karato, 1995; Bystricky et al., 2000; Demouchy et al., 2012; Hansen et al., 2012a, 2012b, 2012c, 2014) and for a natural shear zone in the Josephine peridotite (Warren et al., 2008). For reference, it also displays the evolution of the orientation of the long axis of the finite strain ellipsoid as well as the predictions of tangent and second-order VPSC models (TGT-VPSC and SO-VPSC) without recrystallization.

The experimental data show a strong dispersion, due to variations in the experimental conditions (initial grain sizes, temperature, H_2O fugacity, etc.) that affect the olivine deformation and recrystallization, non-random initial CPOs of the synthetic hot-pressed olivine aggregates (cf. Demouchy et al., 2012), and uncer-

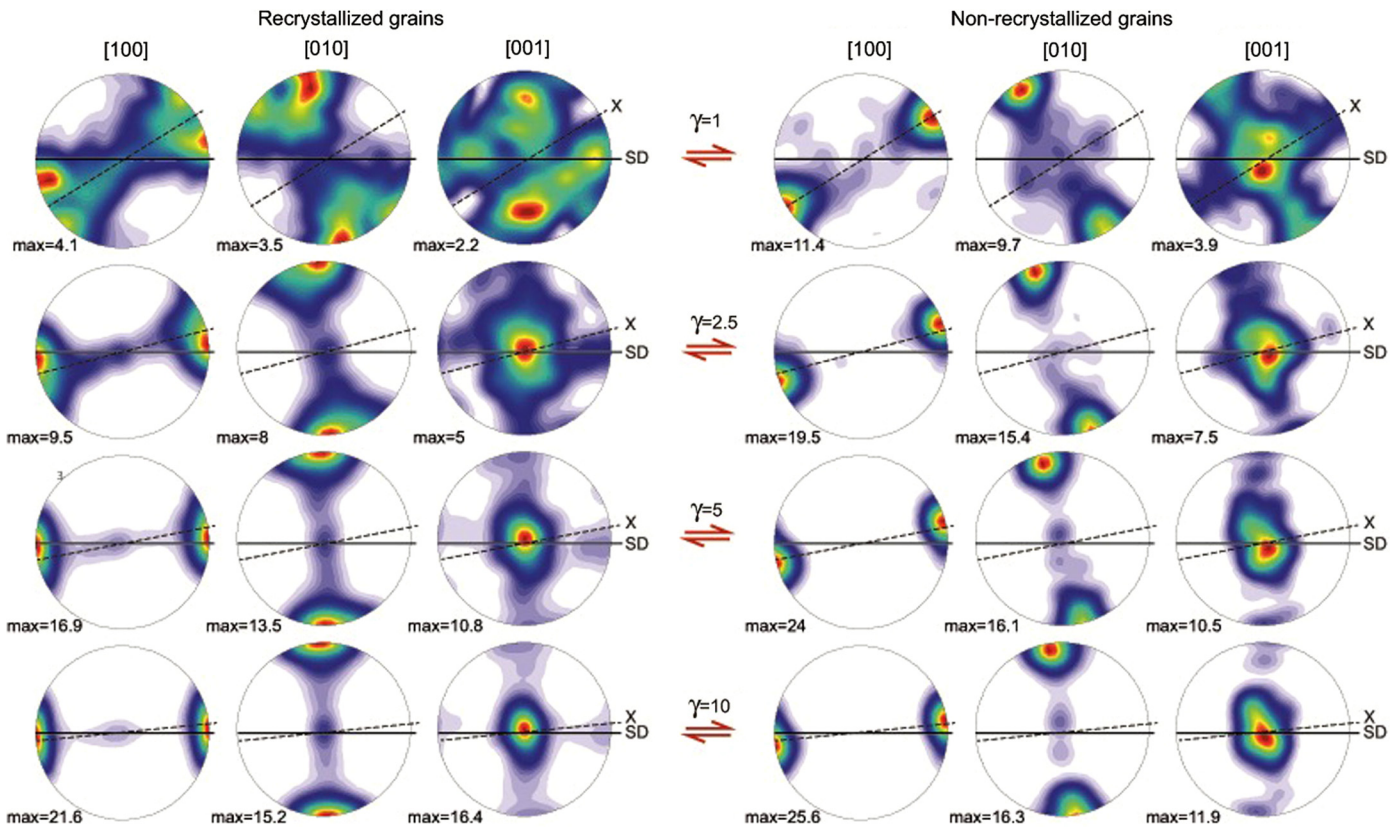

Fig. 3. Comparison between the CPO evolution with increasing shear strain (γ) of recrystallized (in which at least one subgrain nucleation event occurred) and non-recrystallized (in which no subgrains formed) grains; note the faster rotation and the parallelism between the [100] maximum and the shear direction, but slower evolution of the CPO intensity of the recrystallized. Lower hemisphere stereographic plots. SD = shear direction; X = maximum finite stretching direction (lineation); Z = maximum finite shortening direction (normal to the foliation). The continuous black line marks the shear plane, the dashed one, the foliation.

tainties in the determination of the shear direction ($\pm 2°$) and in the CPO measurements ($\pm 1°$). This uncertainty is even higher at low strains, because dispersed CPOs result in poorly determined eigenvectors of the orientation distribution. In addition, some experimental samples show a rotation of the maximum concentration of the olivine [100] axes (characterized by the eigenvector E1 of the orientation distribution) past the shear direction for which there is no clear explanation. In the natural shear zone, the protolith has a well-developed CPO at a high angle to the shear zone orientation. Moreover, the natural shear zone is characterized by coarse-grained peridotites, which contrast with the fine-grained experimental samples. In spite of this, the data shows a clear trend, characterized by a fast rotation of CPO towards a stable orientation characterized by well-developed maxima of [100] and [010] parallel to the shear direction and normal to the shear plane, respectively, which is reached between shear strains of 2–5.

CDRX-CG simulations in which the internal energy is approached by the plastic work rate better reproduce the observations' trend (Fig. 4a). In tangent and second order VPSC simulations the CPO reorientation with increasing shear strain closely follows the finite strain ellipsoid reorientation. The CDRX-CG model in which the internal energy is approached by the plastic work displays an intermediate evolution. However, even in work rate-based CDRX-CG simulations, the stable orientation is achieved at higher shear strains (shear strain ≥ 5) than in most experiments. This is consistent with development of subgrains at very low strains (1–2%) and almost complete recrystallization of experimental samples at strains as low as 2 (Bystricky et al., 2000; Demouchy et al., 2012). The dependence of the reorientation rate of the CPO on the recrystallization rate is coherent with the difference in orientation between recrystallized and non-recrystallized grains (Fig. 3). The faster rotation of the recrystallized grains is consistent with the orientations of recrystallized grains and porphyroclasts in coarse-grained dunites deformed in torsion (cf. Fig. 7 in Skemer et al., 2011).

CDRX-CG models also reproduce better the slow evolution of the intensity of the CPO in the high shear strain experiments, but asymptotic intensities in the models are slightly higher than those observed in the experiments (Fig. 4b). However, CDRX-CG models with more efficient creation of subgrains (lower strain and probability thresholds) or in which strong misorientations between subgrains are permitted (ϑ max. $= \pm 30°$) simulate correctly the moderate strength CPOs displayed by experimentally sheared olivine polycrystals (Supplementary Material Fig. S1k).

5. Role of intragranular strain heterogeneity on the CPO evolution

In the present models, the formation of a subgrain results in both disorientation of part of the crystal and intragranular strain heterogeneity. For discriminating the role of these two processes on the CPO evolution, we run models in which we allow for recrystallization as described in Section 2.1, but treat the mechanical interactions within a grain using the TGT-VPSC approach, instead of the CG one. This results in lower strain heterogeneity among the subgrains that compose a grain and produces a plainly different CPO evolution (CDRX-TGT-VPSC model in Fig. 4). The maximum concentration of [100] follows the orientation of the maximum finite strain ellipsoid axis up to shear strains of 8 (Fig. 4). At higher shear strains, it starts to rotate faster than the finite strain ellipsoid, aligning with the CDRX-CG model at a shear strain of 20. These simulations highlight that the fragmentation of a grain into

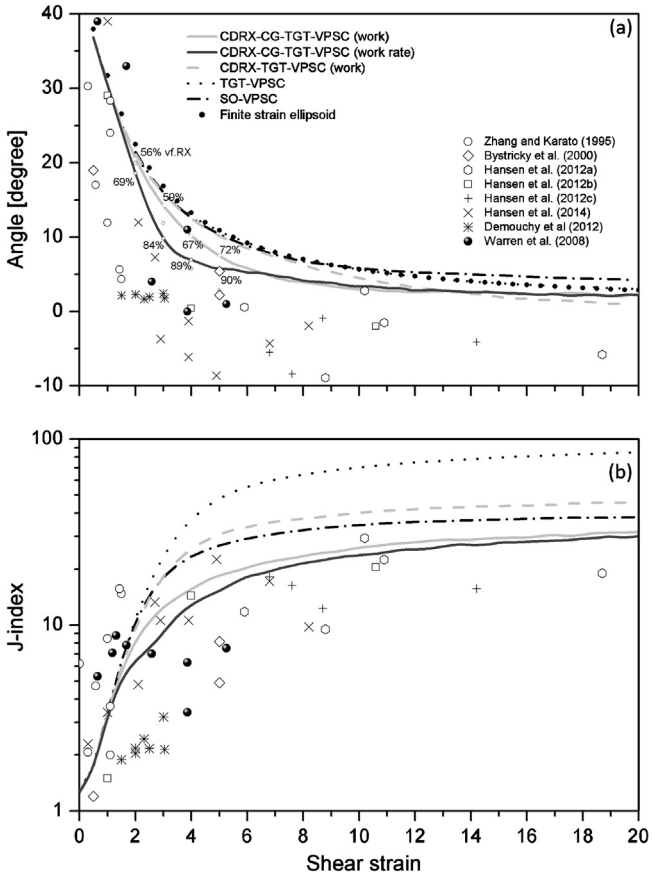

Fig. 4. CPO evolution with increasing shear strain (γ) for the reference CDRX-CG-TGT-VPSC model using work and work rate-based recrystallization criteria, a CDRX model without short range interactions between subgrains (CDRX-TGT-VPSC model), the TGT-VPSC model, the second order VPSC model, in simple shear experiments on olivine polycrystals, and in a shear zone in the Josephine ophiolite. (a) CPO intensity, characterized by the J-index. (b) CPO reorientation, characterized by the angle between the maximum eigenvector of the [100] axis orientation distribution and the shear direction. Slip system data are the same for all models (Table 1). Experimental data points from Zhang and Karato (1995), Bystricky et al. (2000), Demouchy et al. (2012), and Hansen et al. (2012a, 2012b, 2012c, 2014). Data for the Josephine shear zone from Warren et al. Black symbols indicate data obtained at 1200 °C at dry conditions. Grey points mark data obtained at 1300 °C or at wet conditions.

subgrains and the associated dispersion of the crystal orientations do not suffice to decouple the rotation of the CPO from the finite strain ellipsoid one. The relaxation in strain compatibility in the short-range interactions, that is, allowing for strain heterogeneity within the grains, is therefore essential for fast reorientation of the crystals towards easy glide positions. On the other hand, the evolution of the CPO intensity in the CDRX-only model is clearly slower than the TGT-VPSC model (Fig. 4b). This suggests that the CPO dispersion associated with the rotation of the subgrains relative to their parent is the main feature allowing for a slower evolution of the CPO intensity.

The enhanced intragranular strain heterogeneity (relaxed strain compatibility) associated with the formation of subgrains is a thus key factor for producing fast rotation and early stabilization of olivine CPO during simple shear. It allows for a more heterogeneous strain rate distribution in the polycrystal, with a few grains, which are well-oriented to glide on the easy [100](010) system, displaying high shear strains rates (up to 4 times the average one) and a majority of crystals, which are in hard orientations, deforming very slowly (Fig. 5). This strain rate distribution results in high plastic spin rates, similar to the macroscopic ones, for the first population, stabilizing these grains in an orientation in which the [100](010) system is parallel to the macroscopic shear, and in low plastic spin rates for the other crystals, allowing them to be reoriented.

6. Slip systems activity and mechanical behavior of the polycrystal

Since none of the models includes intrinsic hardening, the mechanical behavior of the polycrystal and the slip system activity are mainly controlled by the CPO evolution (geometrical hardening or softening), but they also depend on treatment of the mechanical interactions, which is different for the three models. Fig. 6 compares the evolution of the polycrystal strength with increasing shear strain in work and work rate-based CDRX-CG, TGT-VPSC, and SO models. All models show an initial hardening stage, followed by a marked softening, which evolves towards a quasi-steady state. They differ by: (i) the intensity of the hardening, which is much lower in CDRX-CG models, (ii) the shear strain at which softening starts, which is lower (shear strain of $\sim$2) for both CDRX-CG and SO models, and (iii) the initial rate of softening, which is higher for work rate-based CDRX-CG model, consistently with the more effective subgrain formation. The three models also differ by the 'final' quasi-steady polycrystal stress, which is only 1.5 times the CRSS for the easy [100](010) system in CDRX-CG models. At all strains, polycrystal stresses are much higher in SO models, consistently with predictions of full-field plasticity models like FFT (Castelnau et al., 2008).

The mechanical behavior of the polycrystal is directly linked to the slip systems activity (Fig. 7). Up to a shear strain of 1, all models display a similar behavior, which is consistent with the imposed slip system data (Table 1). The initial drop in the activity of [100](010) is associated with increased activity of the coplanar system [001](010) in both CDRX-CG and the TGT-VPSC models. In the SO-VPSC model this reduction is compensated by the increase of the activity of [100](001). With increasing shear strain, reorientation of the CPO results in increase in the activity of [100](010) up to a value at which it stabilizes. However, the evolution rates and the shear strains at which the slip systems activity becomes stable vary. The CDRX-CG work rate-based model shows the fastest evolution rate and the earliest stabilization of the slip systems activity (at a shear strain of 5). The TGT-VPSC model displays the slowest evolution rate and the latest stabilization of the slip systems activity. In the SO-VPSC model, the rate of increase of the [100](010) activity is intermediate, but the decrease in the activity of the [001](010) system is more marked. This is accompanied by increase in the activity of one of the pyramidal systems, which accounts for the higher polycrystal stresses predicted by this model. The evolution slows down for shear strains higher than 4 and the slip systems' activity stabilizes for shear strains $\geq$6. The lower final activity of the easy [100](010) is consistent with the higher stresses in the SO model.

The evolution of the polycrystal strength in the different models may be compared to mechanical data from simple shear experiments on olivine polycrystals at high temperature conditions (Bystricky et al., 2000; Demouchy et al., 2012; Hansen et al., 2012a, 2012b). Similarly to CPO data, the various mechanical datasets show a strong dispersion, but outline a common trend. The maximum yield stress is attained at low shear strains ($<$1). It is followed by a marked weakening, which evolves into a quasi-stationary behavior. At shear strains of 2–3, shear stresses are reduced by 25–30% relative to the peak value (Bystricky et al., 2000; Demouchy et al., 2012). Stronger weakening (up to a factor 2) is observed at higher shear strains (up to 14.2; Hansen et al., 2012a, 2012b). In addition, comparison of the polycrystalline and single crystal data for olivine Fo90 (Bystricky et al., 2000 and Bai et al., 1991) shows that the steady-state strength of the sheared polycrystals approaches the strength of crystals oriented as to maxi-

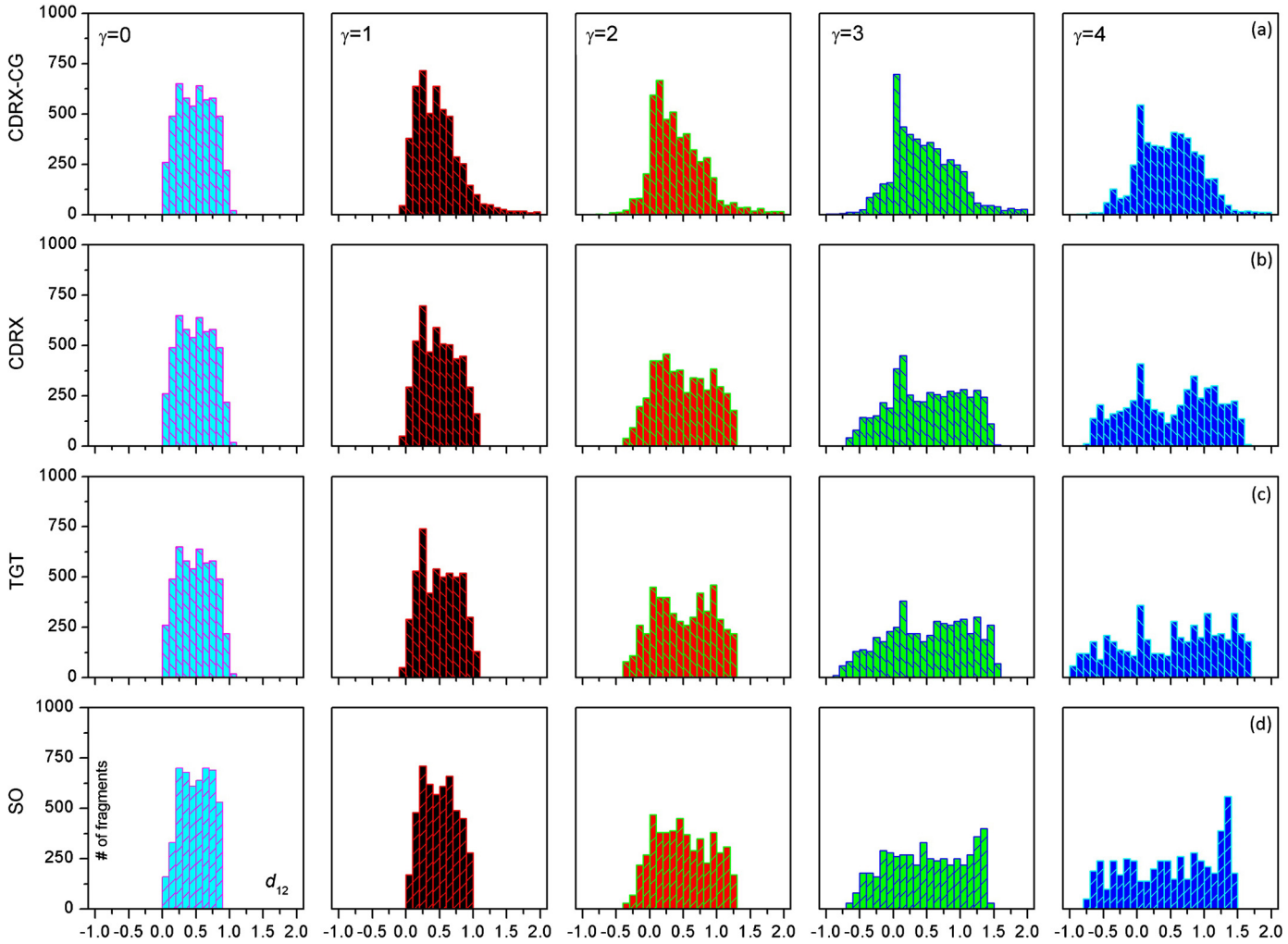

Fig. 5. Evolution of the distribution of the local strain rate d^{g}_{12i} with increasing shear strain for the (a) the CDRX-CG model with a work rate-based nucleation criterion, (b) the CDRX-TGT-VPSC model, (c) the TGT-VPSC model, and (d) the SO-VPSC model.

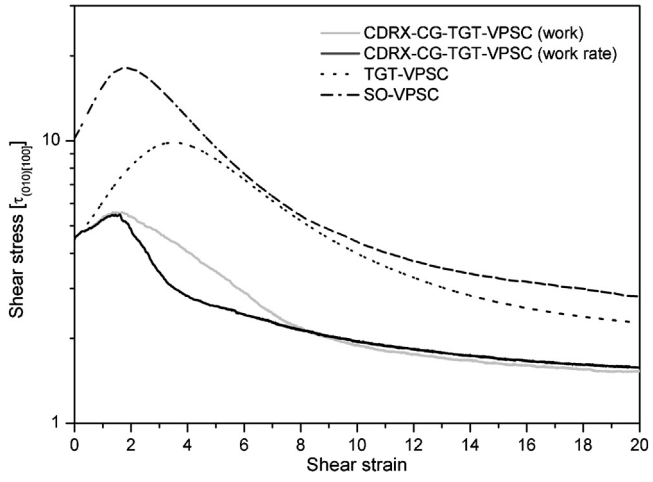

Fig. 6. Evolution of polycrystal shear stress with increasing shear strain for the CDRX-CG model with either a work rate-based or work-based nucleation criterion, the TGT-VPSC model, and the SO-VPSC model.

mize the activation of [100](010). These observations are partially reproduced by the CDRX-CG model: steady state stresses are ~50% lower than the peak ones and 1.5 times the CRSS of the [100](010) system. However, both the weakening and the achievement of a quasi-steady state are shifted towards higher shear strains, consistently with the slower CPO evolution.

7. Predicting olivine CPO evolution in a corner flow

To test the CDRX-CG model for complex flow patterns, we simulated the CPO evolution for the corner flow model used by Castelnau et al. (2009) to compare the predictions of the different existing micromechanical models. The modeled flow pattern aims to represent the mantle flow beneath an oceanic ridge. We analyze the CPO evolution and the slip systems activity along a streamline containing a rapid change on the deformation from vertical upwelling to horizontal shearing. The corresponding velocity gradient history was discretized in incremental steps of 10^5 yrs or less in order to keep the strain increment $\leq$1%; a total of 337 steps were used. The iterative procedure was stopped with a tolerance of 10^{-4}. As in the previous models, the starting texture is a random aggregate of 500 orientations and the slip systems data are listed in Table 1.

The CPOs at different positions along the streamline are presented in Fig. 8, together with the results for TGT-VPSC and SO-VPSC simulations, which are consistent with those reported by Castelnau et al. (2009). The evolution along the vertical is similar in the three models. It is characterized by progressive alignment of the [100] axis with the maximum finite strain ellipsoid axes. Dif-

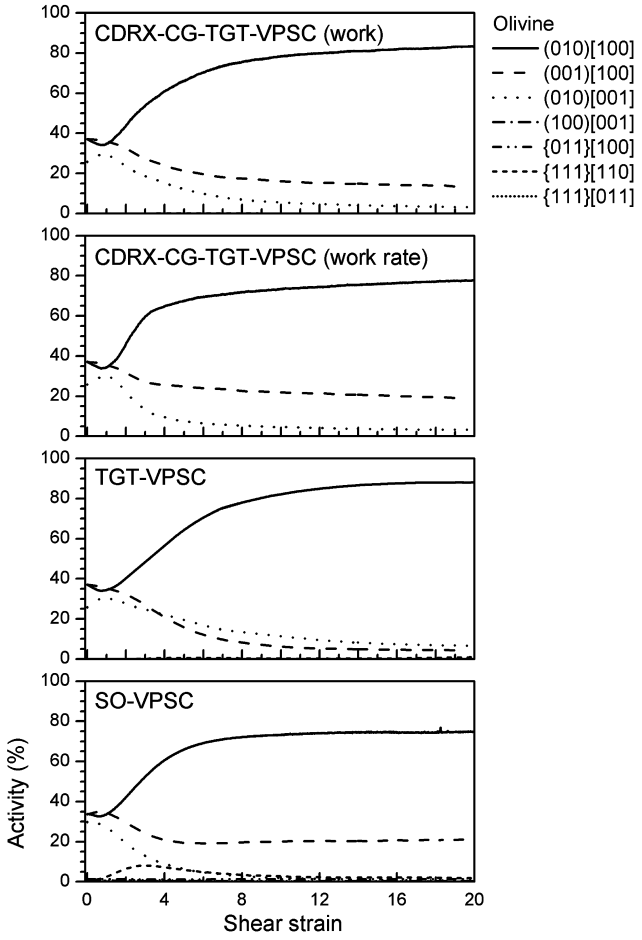

Fig. 7. Evolution of the slip systems activity with increasing shear strain for the CDRX-CG model with either a work rate-based or work-based nucleation criterion, the TGT-VPSC model, and the SO-VPSC model.

ferences between models appear at the start of the flow corner, at ~12 Myr. Both TGT-VPSC and SO-VPSC predict a dispersion of the CPO in the corner, followed by very slow development of a new CPO in the horizontal shear branch, which results in a weak [100] maximum at 34.7° and 35.1° to the horizontal at the end of the simulation, respectively. In contrast, CDRX-CG models predict much less dispersion and faster reorientation of the CPO in the horizontal branch. In work-based simulations, this re-orientation includes the formation of a secondary [100] maximum at low angle to the horizontal flow direction and progressive transfer of weight from the maximum inherited from the previous flow direction. In work-rate based simulations, the re-orientation takes place via an anticlockwise rotation of the entire CPO, which allows for subparallelism of the [100] maximum with the horizontal rapidly after the exit of the corner flow. The difference among these models indicates that in a complex flow the rate of re-orientation of the CPO relative to the rate of change of the deformation field plays an essential role on the final CPO. The more effective formation of subgrains in work-rate based CDRX-CG model results in faster CPO re-orientation rates and less dispersion of the CPO. To further test the importance of the CPO evolution in the corner region, we conducted simulations in which the TGT-VPSC model was used until 16 Myr (that is the end of the corner flow) and then the CDRX-CG model was applied or vice-versa (Supplementary Material Fig. S2). In both cases, the change in the model for the horizontal shearing path does not change significantly the CPO predictions at 24.1 Myr. It is interesting to note that opposite to the evolution observed for simple shear of an initially random polycrystal, where the CDRX-CG model predicts lower CPO strength relatively to the TGT-VPSC model, in a complex flow the CDRX-CG model results in stronger CPO.

We do not have direct observations of the CPO evolution beneath an oceanic ridge, but seismic anisotropy measurements at oceanic ridges, such as the MELT data, show shear wave splitting at stations close to the ridge with fast polarization directions normal to the ridge and strong delay times (Wolfe and Solomon, 1998). Pn data also indicates strong anisotropy with fast propagation parallel to fossil spreading directions in the shallow suboceanic lithospheric mantle (e.g., Raitt et al., 1969). Finally, horizontal foliation sections of ophiolites display strong olivine CPO (e.g., Boudier and Coleman, 1981). All these observations point to preservation and fast re-orientation of olivine CPO after the corner flow, with development of a clear [100] maximum parallel to the spreading direction. They are therefore consistent with the predictions by the CDRX-CG work rate-based model.

8. Conclusions

We propose a simple scheme to model the effects of dynamic recrystallization by subgrain rotation (CDRX) on the CPO evolution. This model simulates both the kinematic (fragmentation of the crystals and misorientation of the subgrains relative to the parent) and the mechanical effects (enhanced intragranular strain heterogeneity and relaxed strain compatibility) of CDRX via a composite grain scheme, in which the short-range interactions (within a grain) follow a constant stress (lower bound) model whereas the long-range interactions (between grains) are modeled by a VPSC approach.

Comparison of the CPO evolution predicted by this model with the results of tangent and second order VPSC models or of a model in which only the kinematic effects of subgrain rotation recrystallization (CDRX) are simulated shows that the enhanced intragranular strain heterogeneity (relaxed strain compatibility) associated with the formation of subgrains is a key factor for producing fast rotation and early stabilization of olivine CPO during simple shear. It also results in marked weakening at low shear strains and the low steady-state stress of the textured aggregates during continued simple shear (<2 times the critical resolved shear stress for the easier [100](010) system). Both predictions are qualitatively consistent with mechanical data for olivine polycrystals deformed in simple shear at high temperature conditions.

In conclusion, the CDRX-CG model better simulates both the CPO evolution in simple shear and its effect on the mechanical behavior of the polycrystal, which are underestimated by tangent VPSC models. The present model is therefore more akin to simulate correctly the effects of texture induced-mechanical anisotropy on the mantle dynamics. In addition, the proposed recrystallization model may be easily implemented in more sophisticated VPSC models, like the SO approach.

Acknowledgements

This work benefited from discussions with A. Vauchez and D. Mainprice. We thank L. Hansen and S. Demouchy for providing previously published EBSD data and O. Castelnau for providing the velocity gradient data for the corner flow benchmarking. D. Mainprice provided software for analyzing and plotting CPO data. The research leading to these results was funded by the projects: Ecos Sud – CONICET A09U01 'Evolution de la texture et de l'anisotropie lors de la déformation haute température des roches et des métaux' and CNRS-CONICET 16064 'Modélisation multi-échelles de la déformation de la lithosphère: anisotropie mécanique et localisation de la déformation'.

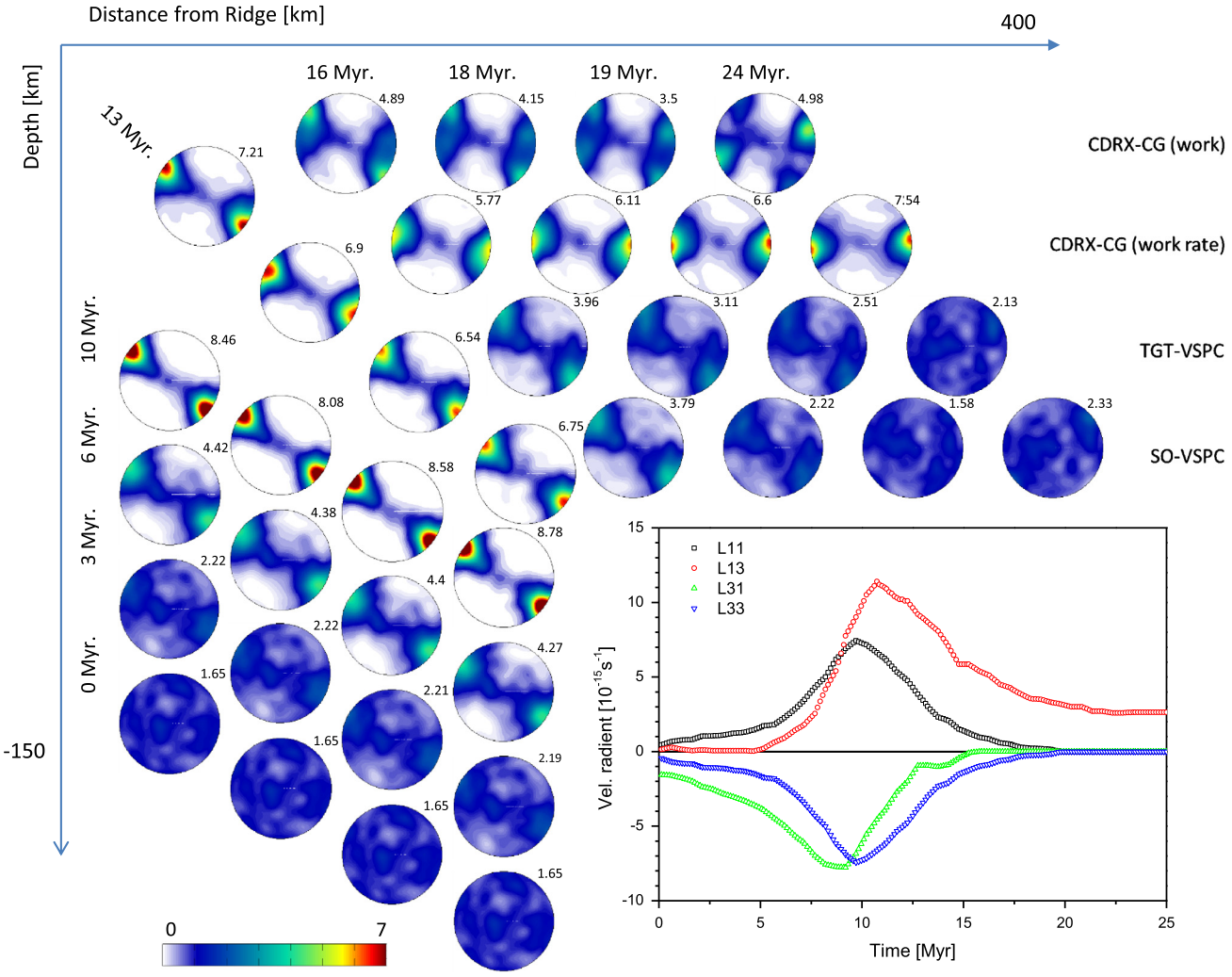

Fig. 8. Predicted CPO evolution for an initially random olivine polycrystal along a typical streamline of a ridge-type corner flow (Castelnau et al., 2009, streamline #1832) for the CDRX-CG with work- and work rate-based nucleation criteria, respectively, the TGT-VPSC, and the SO-VPSC model. Insert shows the evolution of the deformation gradient tensor along the streamline.

Appendix A. Supplementary material

Supplementary material related to this article can be found online at http://dx.doi.org/10.1016/j.epsl.2015.08.018.

References

Bai, Q., Mackwell, S.J., Kohlstedt, D.L., 1991. High-temperature creep of olivine single crystals 1. Mechanical results for buffered samples. J. Geophys. Res. 96, 2441–2463.

Ben Ismaïl, W., Mainprice, D., 1998. An olivine fabric database: an overview of upper mantle fabrics and seismic anisotropy. Tectonophysics 296, 145–157.

Bouchez, J.L., Duval, P., 1982. The fabric of polycrystalline ice deformed in simple shear: experiments in torsion, natural deformation and geometrical interpretation. Texture Stress Microstruct. 5, 171–190.

Boudier, F., Coleman, R.G., 1981. Cross section through the peridotites in the Samail ophiolite, southeastern Oman. J. Geophys. Res. 86, 2573–2592.

Buiskool Toxopeus, J.M.A., Boland, J.N., 1976. Several types of natural deformation in olivine, an electron microscope study. Tectonophysics 32, 209–233.

Bystricky, M., Kunze, K., Burlini, L., Burg, J.P., 2000. High shear strain of olivine aggregates: rheological and seismic consequences. Science 290, 1564–1567.

Castelnau, O., Blackman, D.K., Lebensohn, R.A., Ponte Castañeda, P., 2008. Micromechanical modeling of the viscoplastic behavior of olivine. J. Geophys. Res. 113, B09202.

Castelnau, O., Blackman, D.K., Becker, T.W., 2009. Numerical simulations of texture development and associated rheological anisotropy in regions of complex mantle flow. Geophys. Res. Lett. 36, L12304.

Chai, M., Brown, J.M., Slutsky, L.J., 1996. Thermal diffusivity of mantle minerals. Phys. Chem. Miner. 23, 470–475.

Chastel, Y.B., Dawson, P.R., Wenk, H.R., Bennett, K., 1993. Anisotropic convection with implications for the upper mantle. J. Geophys. Res. 98, 17757–17771.

Dell'Angelo, L.N., Tullis, J., 1989. Fabric development in experimentally sheared quartzites. Tectonophysics 169, 1–21.

Demouchy, S., Tommasi, A., Barou, F., Mainprice, D., Cordier, P., 2012. Deformation of olivine in torsion under hydrous conditions. Phys. Earth Planet. Inter. 202, 56–70.

Demouchy, S., Tommasi, A., Boffa Ballaran, T., Cordier, P., 2013. Low strength of Earth's uppermost mantle inferred from tri-axial deformation experiments on dry olivine crystals. Phys. Earth Planet. Inter. 220, 37–49.

Durham, W.B., Goetze, C., 1977. Plastic flow of oriented single crystals of olivine: 1. Mechanical data. J. Geophys. Res. 82, 5737–5753.

Etchecopar, A., 1977. A plane kinematic model of progressive deformation in a polycrystalline aggregate. Tectonophysics 39, 121–139.

Etchecopar, A., Vasseur, G., 1987. A 3-D kinematic model of fabric development in polycrystalline aggregates: comparisons with experimental and natural examples. J. Struct. Geol. 9, 705–717.

Falus, G., Tommasi, A., Soustelle, V., 2011. The effect of dynamic recrystallization on olivine crystal preferred orientations in mantle xenoliths deformed under varied stress conditions. J. Struct. Geol. 33, 1528–1540.

Gourdet, S., Montheillet, F., 2003. A model of continuous dynamic recrystallization. Acta Mater. 51, 2685–2699.

Green II, H.W., Radcliffe, S.V., 1972. Dislocation mechanisms in olivine and flow in the upper mantle. Earth Planet. Sci. Lett. 15, 239–247.

Grennerat, F., Montagnat, M., Castelnau, O., Vacher, P., Moulinec, H., Suquet, P., Duval, P., 2012. Experimental characterization of the intragranular strain field in columnar ice during transient creep. Acta Mater. 60, 3655–3666.

Guillope, M., Poirier, J.P., 1979. Dynamic recrystallization during creep of single-crystalline halite: an experimental study. J. Geophys. Res. 84, 5557–5567.

Hansen, L.N., Dillman, A.M., Zimmerman, M.E., Kohlstedt, D.L., 2012c. Strain localization in olivine aggregates at high temperature: an experimental comparison of constant-strain rate and constant-stress boundary conditions. Earth Planet. Sci. Lett. 333–334, 134–145.

Hansen, L.N., Zimmerman, M.E., Kohlstedt, D.L., 2012a. Laboratory measurements of the viscous anisotropy of olivine aggregates. Nature 492, 415–418.

Hansen, L.N., Zimmerman, M.E., Kohlstedt, D.L., 2012b. The influence of microstructure on deformation of olivine in the grain-boundary sliding regime. J. Geophys. Res. 117, B09201.

Hansen, L.N., Zhao, Y.H., Zimmerman, M.E., Kohlstedt, D.L., 2014. Protracted fabric evolution in olivine: implications for the relationship among strain, crystallographic fabric, and seismic anisotropy. Earth Planet. Sci. Lett. 387, 157–168.

Honneff, H., Mecking, H., 1981. Analysis of the deformation texture at different rolling conditions. In: Proceedings of ICOTOM, vol. 6, pp. 347–355.

Jung, H., Karato, S.I., 2001. Water-induced fabric transitions in olivine. Science 293, 1460–1463.

Kaminski, E., Ribe, N.M., 2001. A kinematic model for recrystallization and texture development in olivine polycrystals. Earth Planet. Sci. Lett. 189, 253–267.

Knoll, M., Tommasi, A., Logé, R., Signorelli, J., 2009. A multi-scale approach to model the anisotropic deformation of lithospheric plates. Geochem. Geophys. Geosyst. 10, Q08009. http://dx.doi.org/10.1029/2009GC002423.

Kobayashi, Y., 1974. Anisotropy of thermal diffusivity in olivine, pyroxene, and dunite. J. Phys. Earth 22, 359–373.

Lebensohn, R., Tomé, C., 1993. A self-consistent approach for the simulation of plastic deformation and texture development of polycrystals: application to Zr alloys. Acta Metall. Mater. 41 (9), 2611–2624.

Lebensohn, R., Uhlenhut, H., Hartig, C., Mecking, H., 1998. Plastic flow of γ-tial-based polysynthetically twinned crystals: micromechanical modeling and experimental validation. Acta Mater. 46 (13), 4701–4709.

Mainprice, D., 2007. Seismic anisotropy of the deep Earth from a mineral and rock physics perspective. In: Treatise of Geophysics, vol. 2, pp. 437–491.

Mainprice, D., Tommasi, A., Couvy, H., Cordier, P., Frost, D.J., 2005. Pressure sensitivity of olivine slip systems and seismic anisotropy of Earth's upper mantle. Nature 433, 731–733.

Nicolas, A., Boudier, F., Boullier, A.M., 1973. Mechanisms of flow in naturally and experimentally deformed peridotites. Am. J. Sci. 273, 853–876.

Poirier, J.P., Nicolas, A., 1975. Deformation-induced recrystallization due to progressive misorientation of subgrains, with special reference to mantle peridotites. J. Geol. 83, 707–720.

Proust, G., Tomé, C.N., Kaschner, G.C., 2007. Modeling texture, twinning and hardening evolution during deformation of hexagonal materials. Acta Mater. 55, 2137–2148.

Raitt, R.W., Shor, G.G., Francis, T.J.G., Morris, G.B., 1969. Anisotropy of the Pacific upper mantle. J. Geophys. Res. 74, 3095–3109.

Raterron, P., Detrez, F., Castelnau, O., Bollinger, C., Cordier, P., Merkel, S., 2014. Multiscale modeling of upper mantle plasticity: from single-crystal rheology to multiphase aggregate deformation. Phys. Earth Planet. Inter. 228, 232–243.

Ribe, N.M., 1989. A continuum theory for lattice preferred orientation. Geophys. J. Int. 97, 199–207.

Schmid, S.M., Casey, M., 1986. Complete fabric analysis of some commonly observed quartz c-axis patterns. In: Mineral and Rock Deformation: Laboratory Studies: The Paterson Volume, pp. 263–286.

Skemer, P., Sundberg, M., Hirth, G., Cooper, R., 2011. Torsion experiments on coarse-grained dunite: implications for microstructural evolution when diffusion creep is suppressed. Geol. Soc. (Lond.) Spec. Publ. 360 (1), 211–223.

Solas, D.E., Tomé, C.N., Engler, O., Wenk, H.R., 2001. Deformation and recrystallization of hexagonal metals: modeling and experimental results for zinc. Acta Mater. 49, 3791–3801.

Soustelle, V., Tommasi, A., Demouchy, S., Ionov, D.A., 2010. Deformation and fluid–rock interaction in the supra-subduction mantle: microstructures and water contents in peridotite xenoliths from the Avacha Volcano, Kamchatka. J. Petrol. 51, 363–394.

Tommasi, A., Gibert, B., Seipold, U., Mainprice, D., 2001. Anisotropy of thermal diffusivity in the upper mantle. Nature 411, 783–786.

Tommasi, A., Knoll, M., Vauchez, A., Signorelli, J.W., Thoraval, C., Logé, R., 2009. Structural reactivation in plate tectonics controlled by olivine crystal anisotropy. Nat. Geosci. 2, 423–427.

Tommasi, A., Mainprice, D., Canova, G., Chastel, Y., 2000. Viscoplastic self-consistent and equilibrium-based modeling of olivine lattice preferred orientations: implications for the upper mantle seismic anisotropy. J. Geophys. Res. 105, 7893–7908.

Tommasi, A., Tikoff, B., Vauchez, A., 1999. Upper mantle tectonics: three-dimensional deformation, olivine crystallographic fabrics and seismic properties. Earth Planet. Sci. Lett. 168, 173–186.

Tommasi, A., Vauchez, A., Ionov, D.A., 2008. Deformation, static recrystallization, and reactive melt transport in shallow subcontinental mantle xenoliths (Tok Cenozoic volcanic field, SE Siberia). Earth Planet. Sci. Lett. 272, 65–77.

Warren, J.M., Hirth, G., Kelemen, P.B., 2008. Evolution of olivine lattice preferred orientation during simple shear in the mantle. Earth Planet. Sci. Lett. 272, 501–512.

Wenk, H.R., Bennett, K., Canova, G.R., Molinari, A., 1991. Modelling plastic deformation of peridotite with the self-consistent theory. J. Geophys. Res. 96, 8337–8349.

Wenk, H.R., Tomé, C.N., 1999. Modeling dynamic recrystallization of olivine aggregates deformed in simple shear. J. Geophys. Res. 104, 25513–25527.

Wolfe, C.J., Solomon, S.C., 1998. Shear-wave splitting and implications for mantle flow beneath the MELT region of the East Pacific Rise. Science 280, 1230–1232.

Zaffarana, C., Tommasi, A., Vauchez, A., Grégoire, M., 2014. Microstructures and seismic properties of south Patagonian mantle xenoliths (Gobernador Gregores and Pali Aike). Tectonophysics 621, 175–197.

Zhang, S., Karato, S.I., 1995. Lattice preferred orientation of olivine aggregates deformed in simple shear. Nature 375, 774–777.

Zhang, S., Karato, S.I., Fitz Gerald, J., Faul, U.H., Zhou, Y., 2000. Simple shear deformation of olivine aggregates. Tectonophysics 316, 133–152.